Supplementary Information

Synthesis of ZIF-62 Glass and Solid-state Lithium Superconductor Composite Membranes for Electrodialytic Lithium Extraction

Liang Feng[1, †], Shuhao An[1, †], Xin Wang[1], Yanxiong Ren[1], Shumei Wang[1], Xiaole Li[2], Gilles Lubineau[2], Zhen Li[1, *], Ben Hang Yin[3, *], Zhiping Lai[1, *]

[1] Center of Excellence for Renewable Energy and Storage Technologies, Division of Physical Science and Engineering, King Abdullah University of Science and Technology (KAUST), Thuwal, 23955-6900, Kingdom of Saudi Arabia

[2] Mechanics of Composites for Energy and Mobility Lab, Division of Physical Science and Engineering, King Abdullah University of Science and Technology (KAUST), Thuwal, 23955-6900, Kingdom of Saudi Arabia

[3] The MacDiarmid Institute for Advanced Materials and Nanotechnology, Department of Chemical and Process Engineering, University of Canterbury, Christchurch, 8140, New Zealand

[†] These authors contributed equally

[*] Corresponding author: Z. Li (zhen.li@kaust.edu.sa), B. Yin (ben.yin@canterbury.ac.nz) and Z. Lai (zhiping.lai@kaust.edu.sa)

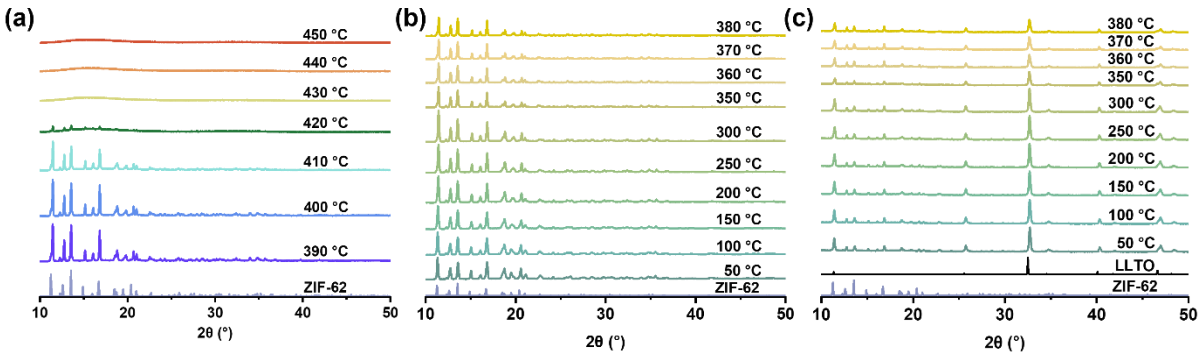

Fig. S1. In-situ XRD of (a) ZIF-62 from 390 °C to 450 °C. (b) ZIF-62 and (c) $(LLTO)_{0.4}(ZIF\text{-}62\ glass)_{0.6}$ from 50 °C to 380 °C.

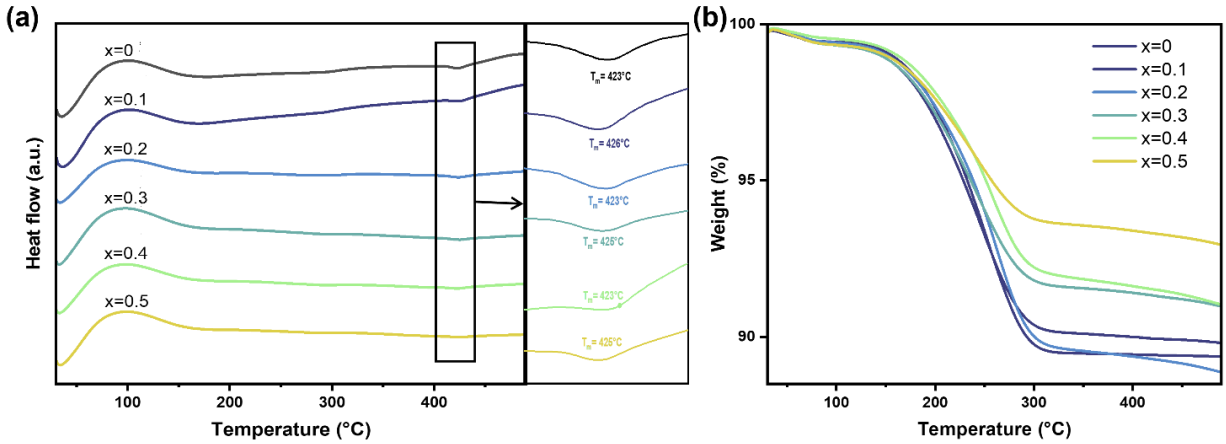

Fig. S2. (a) DSC, and (b) TG curves of $(LLTO)_x(ZIF\text{-}62\ glass)_{1-x}$ pre-mixtures.

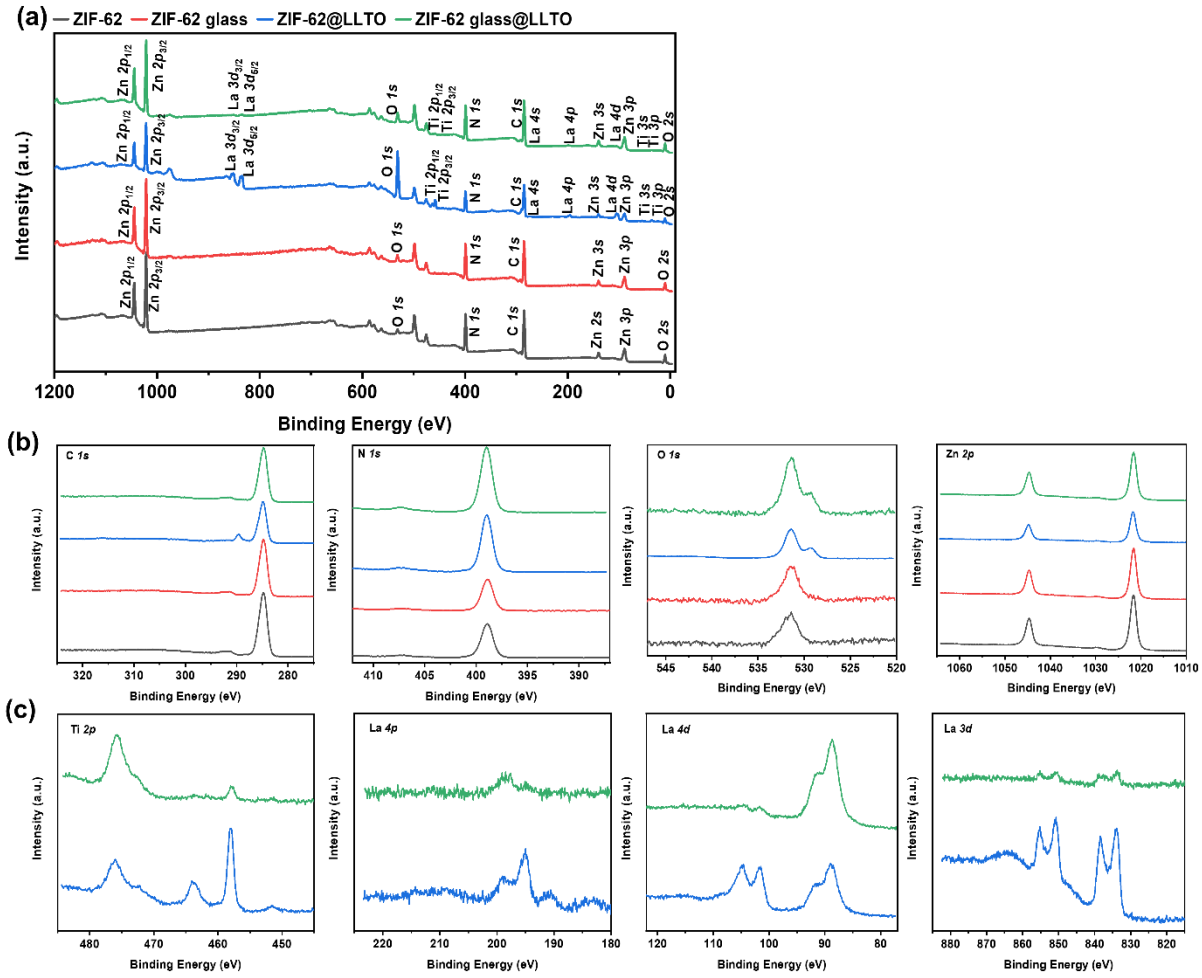

Fig. S3. XPS analysis of ZIF-62, LLTO, and composite samples before (ZIF-62@LLTO) and after (ZIF-62 glass@LLTO) thermal treatment. (a) Survey spectra comparing the elemental composition across all samples. The attenuated LLTO signals are consistent with surface coverage by the glass matrix. (b) High-resolution spectra of framework-related elements for all samples. (c) High-resolution spectra of LLTO-related elements for LLTO-containing samples.

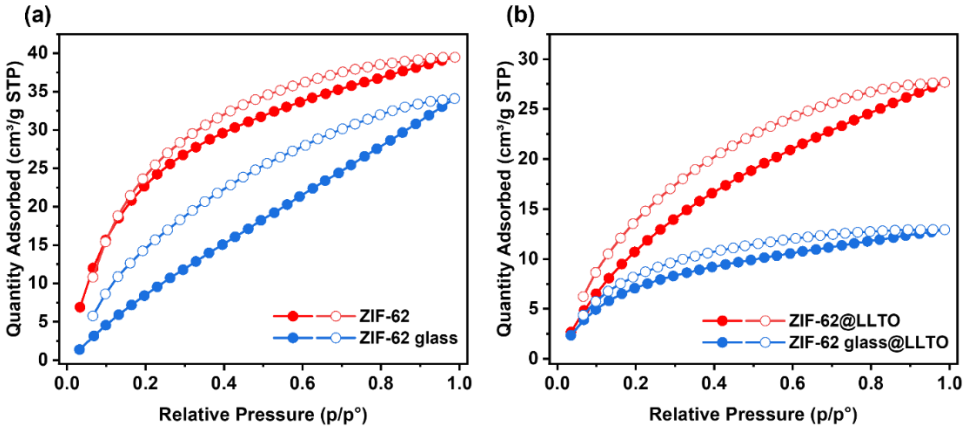

Fig. S4. CO_2 gas sorption isotherms of (a) crystal ZIF-62 and melted ZIF-62 glass. (b) ZIF-62@LLTO and ZIF-62 glass@LLTO.

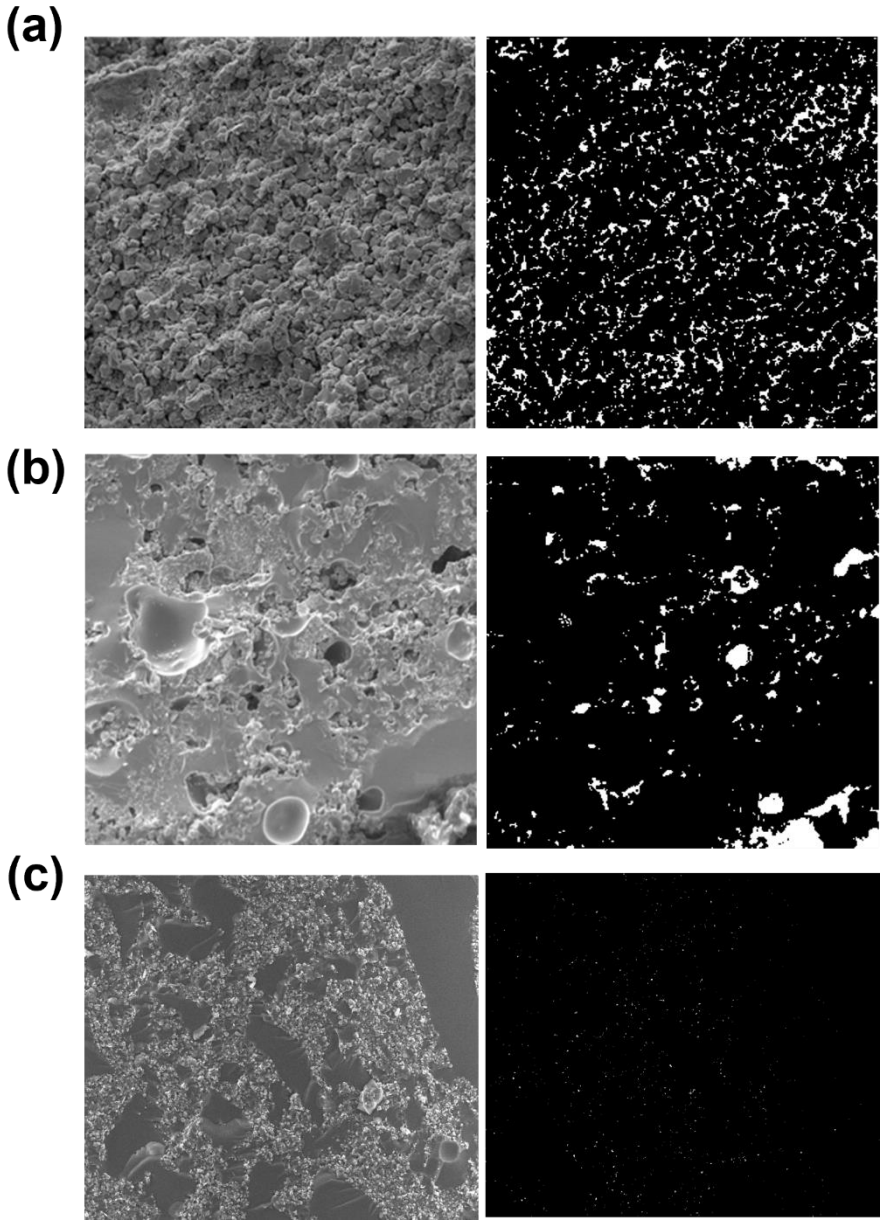

Fig. S5. **Quantitative analysis of temperature-driven structural densification behavior.** Cross-sectional SEM (left) and corresponding processed binary images (right) of the x=0.3 composite membranes fabricated at (a) 350 °C, (b) 400 °C, and (c) 450 °C.

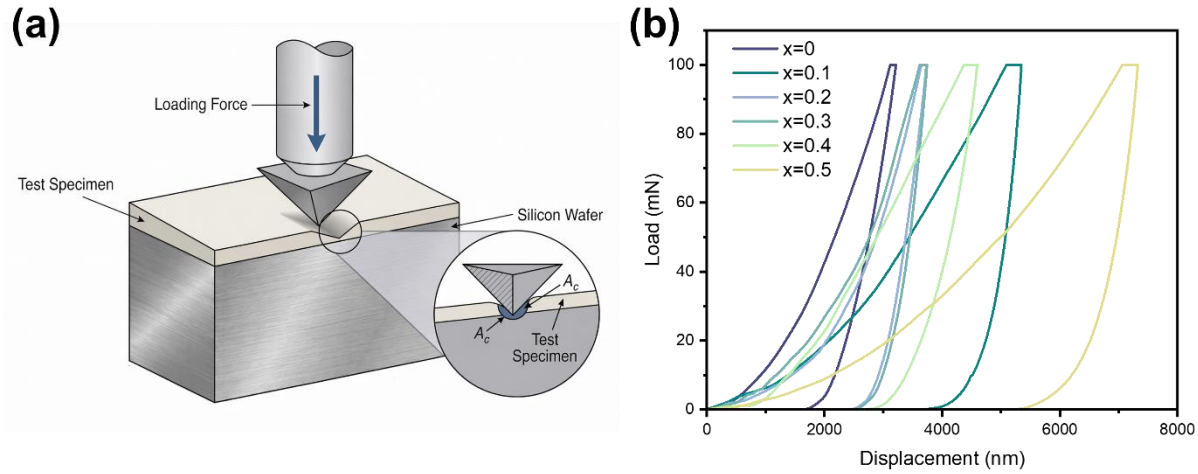

Fig. S6. Microscopic mechanical properties. (a) Schematic illustration of the nanoindentation test. (b) Load–displacement curves for $(LLTO)_x(ZIF\text{-}62\ glass)_{1-x}$ composite membranes under 100 mN maximum load.

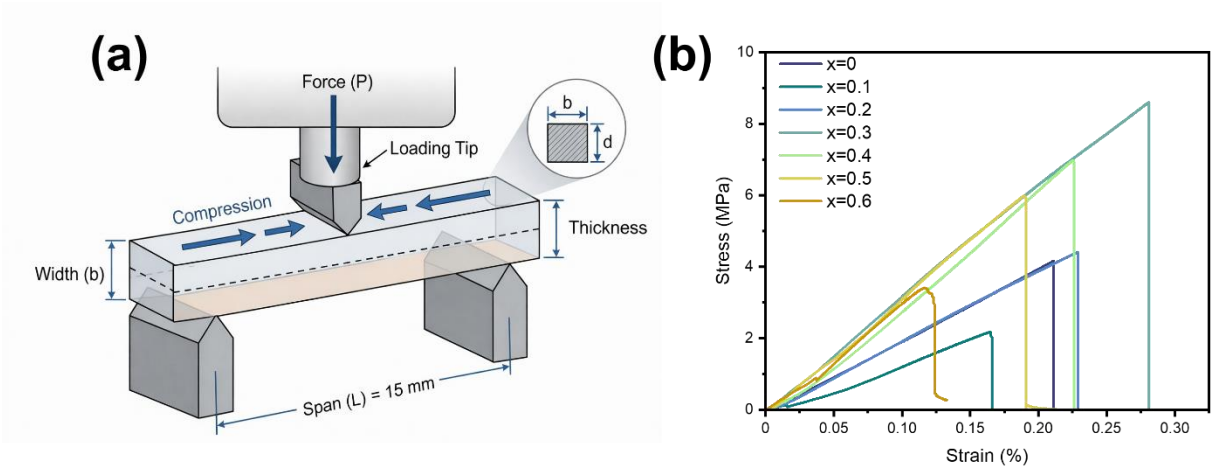

Fig. S7. **Macroscopic mechanical properties.** (a) Schematic illustration of 3-point bending test. (b) Stress-strain curves of the $(LLTO)_x(ZIF\text{-}62\ glass)_{1-x}$ composites obtained from three-point bending tests.

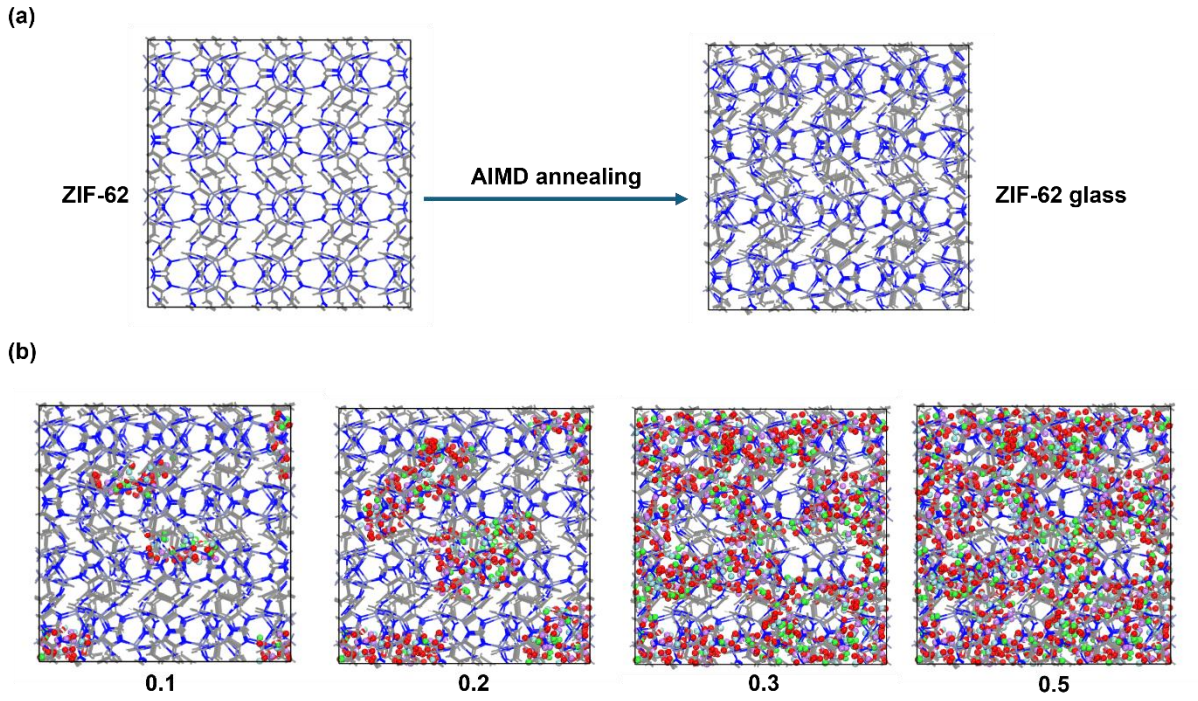

Fig. S8. Structural models of $(LLTO)_x(ZIF\text{-}62\ glass)_{1-x}$ membranes. (a) Structural evolution of ZIF-62 from the crystalline phase to the amorphous glass model used in the simulations via AIMD annealing. (b) Representative snapshots of the composite models with varying LLTO contents (x = 0.1, 0.2, 0.3, and 0.5), showing the spatial distribution of the LLTO phase within the amorphous ZIF-62 glass matrix. The atoms are color-coded as follows: Li (purple), La (light blue), Ti (light cyan), O (red), Zn (bluish gray), N (dark blue), C (gray), H (white), and Cl (green).

The dependence of ionic conductivity on LLTO content was fitted using a classical percolation model[1]:

$$\sigma = A(\psi - \psi_c)^t \qquad (1)$$

where σ is the ionic conductivity, ψ is the LLTO volume fraction, and A, ψ_c, and t are fitting parameters. To correlate the mass fraction (x, wt%) discussed in the main text with the volume fraction (ψ) used in the percolation model, the conversion was performed based on the respective theoretical crystallographic densities of the two initial phases:

$$\psi = \frac{\frac{x}{\rho_{LLTO}}}{\frac{x}{\rho_{LLTO}} + \frac{1-x}{\rho_{glass}}} \qquad (2)$$

where ρ_{LLTO} and ρ_{glass} are the densities of the LLTO ceramic (5.1g cm^{-3})[2] and ZIF-62 (1.35g cm^{-3})[3], respectively. The corresponding fitting results are shown in Fig. S9, exhibiting a high fitting quality ($R^2 \approx 0.991$).

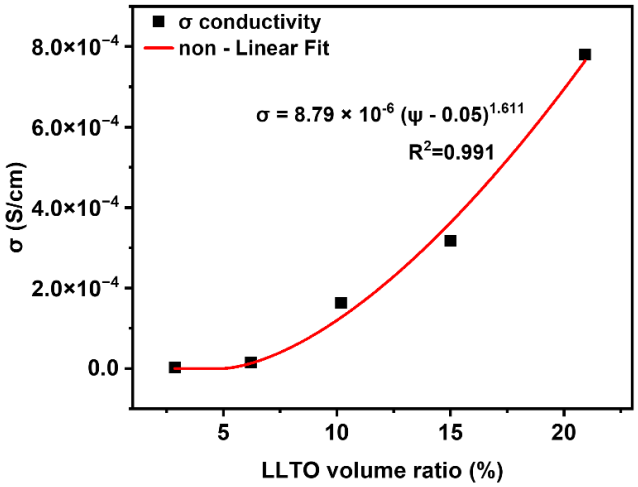

Fig. S9. Ionic conductivity of $(LLTO)_x(ZIF\text{-}62\ glass)_{1-x}$ membranes as a function of LLTO volume fraction, together with a non-linear fit based on percolation theory.

The temperature dependence of ionic conductivity at low LLTO contents (x = 0.1 and 0.2) was analyzed using the Vogel–Tammann–Fulcher (VTF) relation as below[4],

$$\sigma = Ae^{-B/(T-T_0)} \qquad (3)$$

where σ is the ionic conductivity, A is the pre-exponential factor, B is the pseudo-activation energy parameter associated with the ion transport, T is the absolute testing temperature, and T_0 is the Vogel temperature. This model is commonly used to describe non-Arrhenius transport behavior in disordered systems. The corresponding fitting results are presented in Fig. S10.

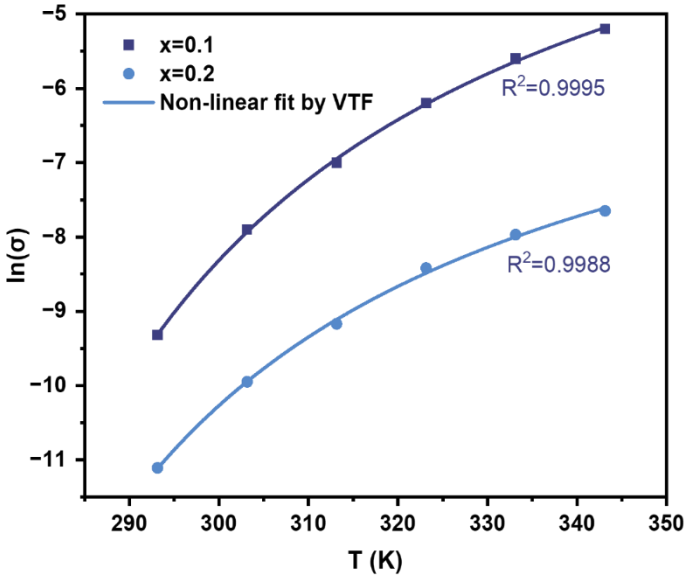

Fig.S10. Temperature-dependent ionic conductivity of $(LLTO)_x(ZIF\text{-}62\ glass)_{1-x}$ membranes at low LLTO contents (x = 0.1 and 0.2), together with VTF fits. The excellent agreement ($R^2 > 0.99$) indicates a non-Arrhenius transport behavior associated with structural relaxation within the glass-dominated composite matrix.

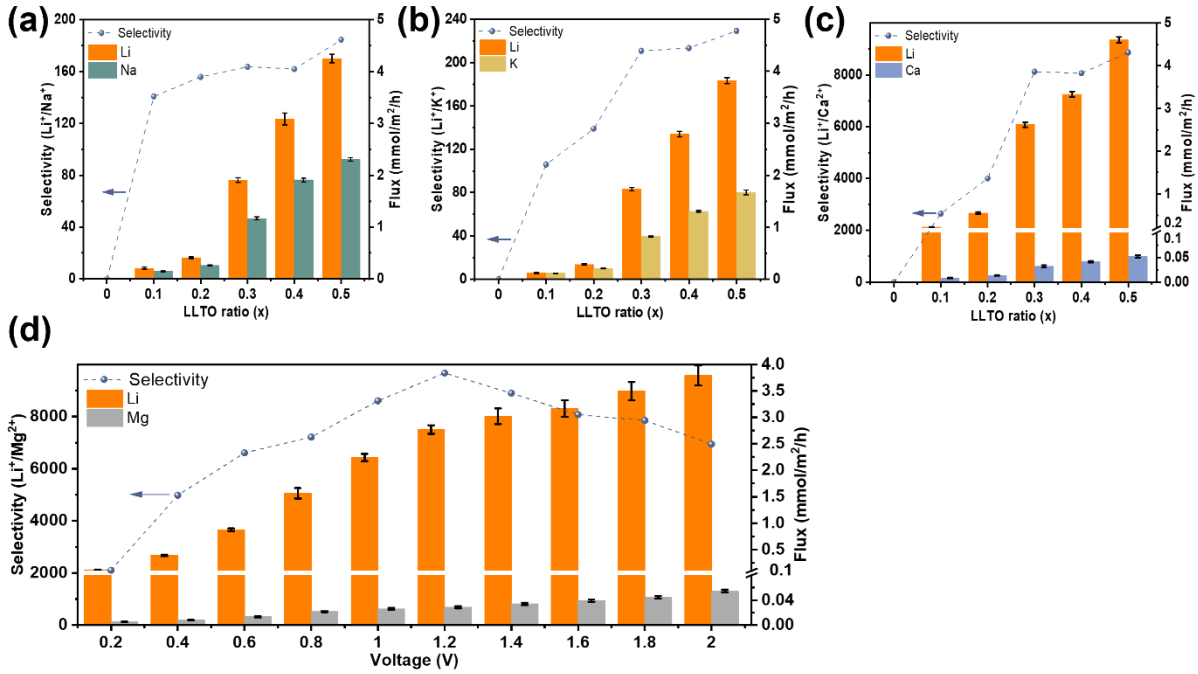

Fig. S11. Flux and selectivity of the $(LLTO)_x$ $(ZIF\text{-}62\ glass)_{1-x}$ in binary metal systems of (a) Li/Na, (b) Li/K, (c) Li/Ca with a molar ratio of 1:100. (d) Influence of voltage in a binary metal system of Li/Mg with a molar ratio of 1:100. Error bars represent standard deviation (SD) from repeated measurements.

The flux of each sample was normalized to a standard baseline thickness of 100 μm using the following equation:

$$J_{normalized} = \frac{J_{measured} \times d_{actual}}{100\mu m} \quad (4)$$

where $J_{measured}$ is the experimentally measured raw flux, and d_{actual} is the actual measured thickness of the tested membrane in μm. The actual thickness of the prepared membranes was accurately measured using a digital micrometer.

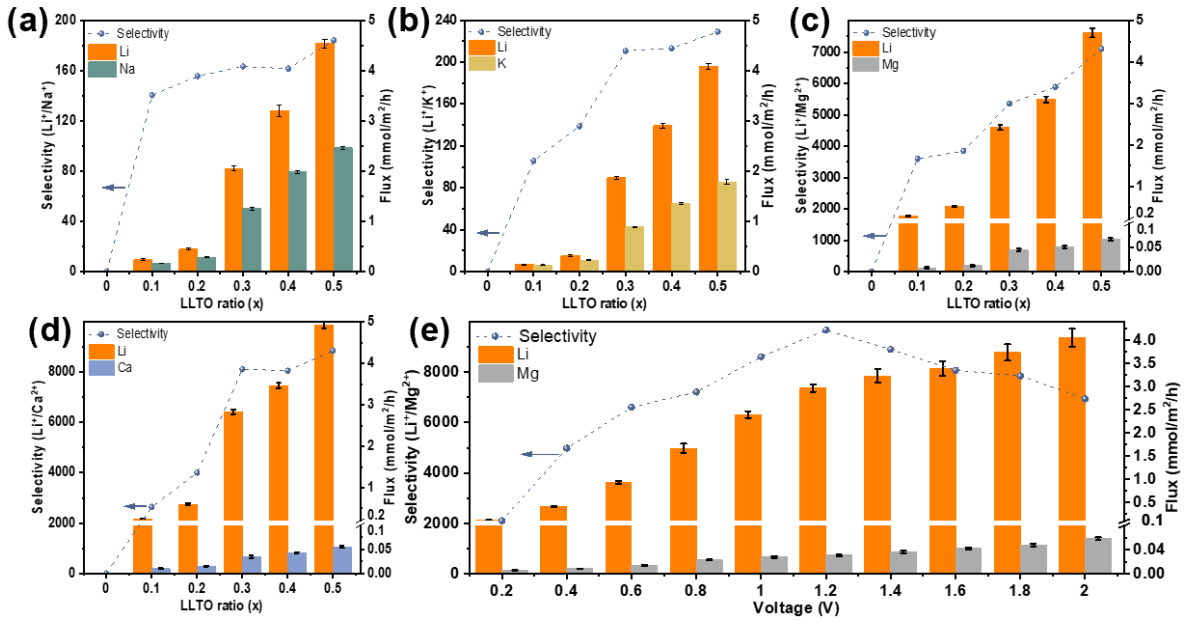

Fig. S12. Thickness-normalized lithium extraction performance in binary systems. The normalized results exhibit consistent trends with the unnormalized data. Error bars represent standard deviation (SD) from repeated measurements.

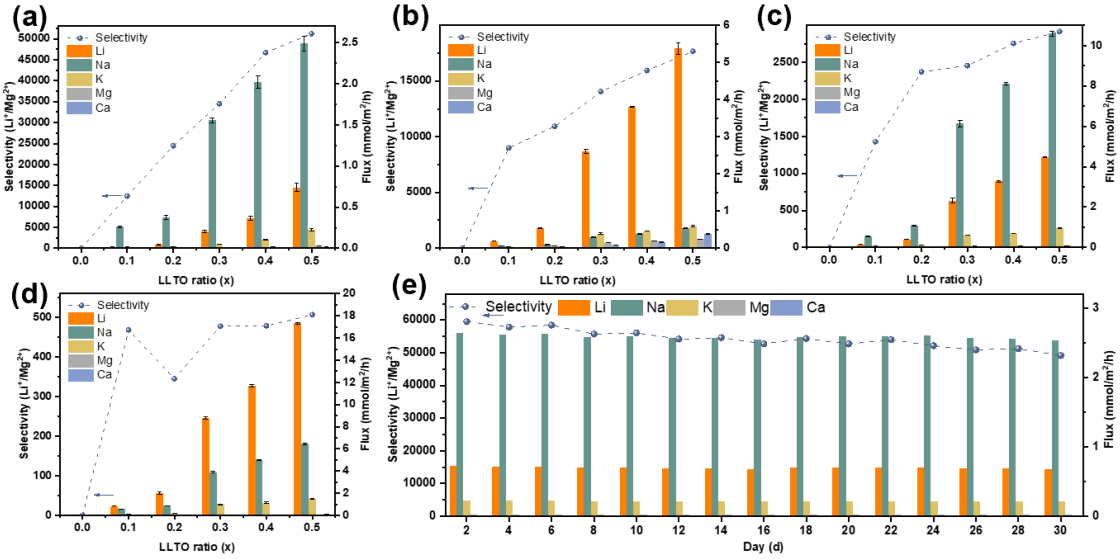

Fig. S13. Thickness-normalized lithium extraction performance in real brines. The normalized results exhibit consistent trends as the unnormalized data. Error bars represent standard deviation (SD) from repeated measurements.

The theoretical charge associated with ion transport was calculated from the measured ion fluxes of the five major cations (Li^+, Na^+, K^+, Mg^{2+}, and Ca^{2+}) according to:

$$Q = FAt(J_{Li} + J_{Na} + J_K + 2J_{Mg} + 2J_{Ca}) \quad (5)$$

where Q is the theoretical charge carried by the transported cations (C), F is the Faraday constant (96485 C mol^{-1}), A is the effective membrane area (m^2), t is the extraction time (h), and J_{Me} is the experimentally measured ion flux (mol m^{-2} h^{-1}) of the corresponding ion. The factor of 2 accounts for the divalent charge of Mg^{2+} and Ca^{2+}.

The Faradaic (current) efficiency was calculated by comparing the theoretical charge associated with ion transport with the total charge passed through the electrochemical cell:

$$\eta_F = \frac{Q}{\int_0^t I(t)dt} \times 100\% \quad (6)$$

where η_F is the Faradaic efficiency (%), I(t) is the measured current (A), and $\int_0^t I(t)dt$ represents the total charge passed through the cell during the extraction process.

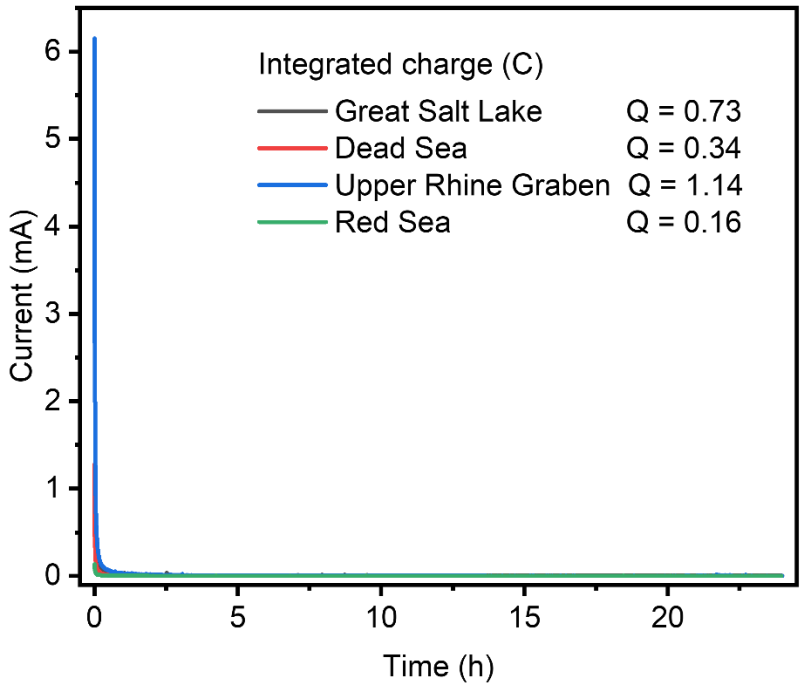

Fig. S14. Current–time responses during lithium extraction from four representative natural brines using the $(LLTO)_{0.5}(ZIF\text{-}62\ glass)_{0.5}$ membrane. Current–time curves recorded during lithium extraction from Red Sea water, Dead Sea brine, Great Salt Lake brine, and Upper Rhine Graben brine. The integrated charge passed through the cell during the 24 h extraction is indicated in the legend. Comparison of the integrated charge with the theoretical ionic charge yielded consistently high Faradaic efficiencies (94.6–95.6%) across all four brine systems.

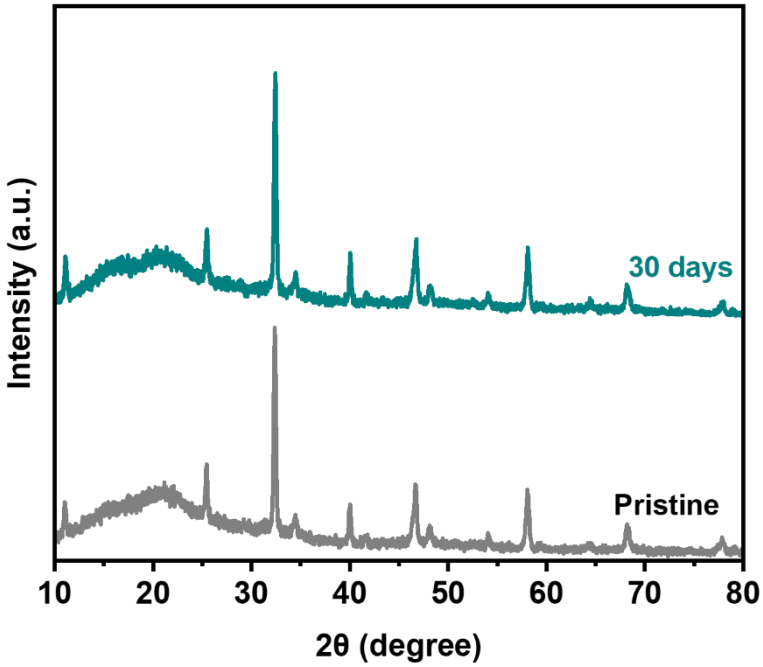

Fig. S15. XRD patterns of the membrane before and after 30 days of durability testing.

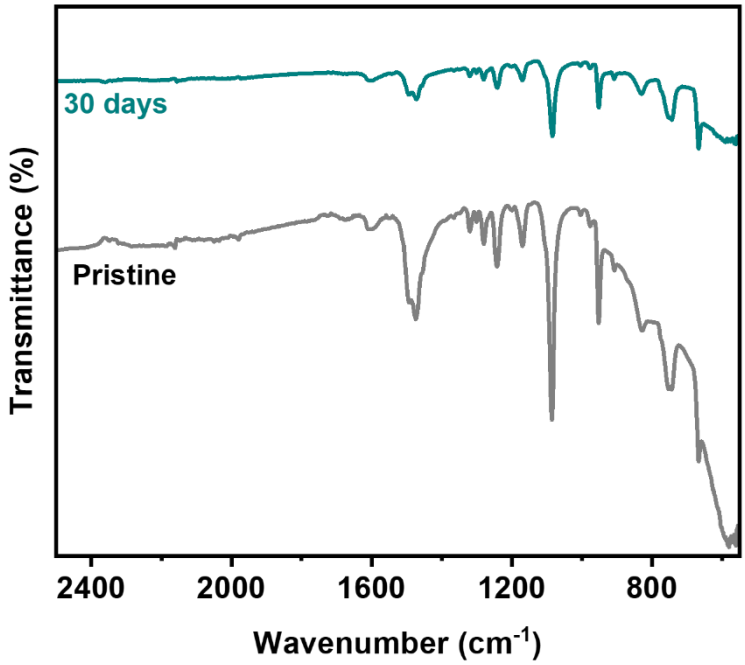

Fig. S16. FTIR patterns of the membrane before and after 30 days of durability testing.

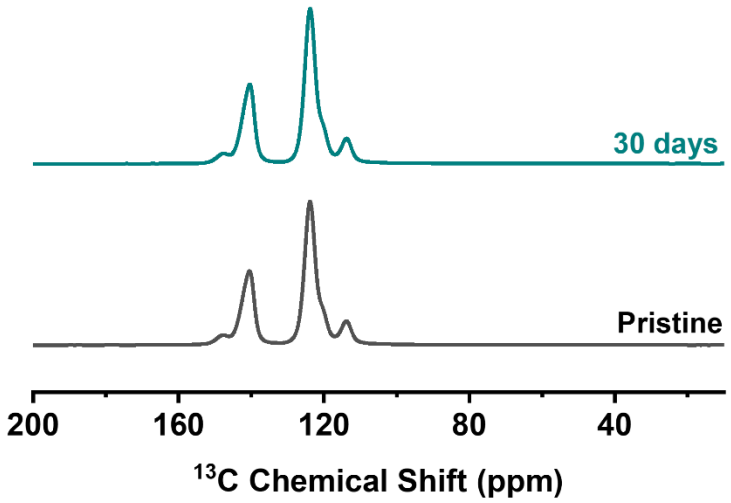

Fig. S17. Solid state NMR of the membrane before and after 30 days of durability testing.

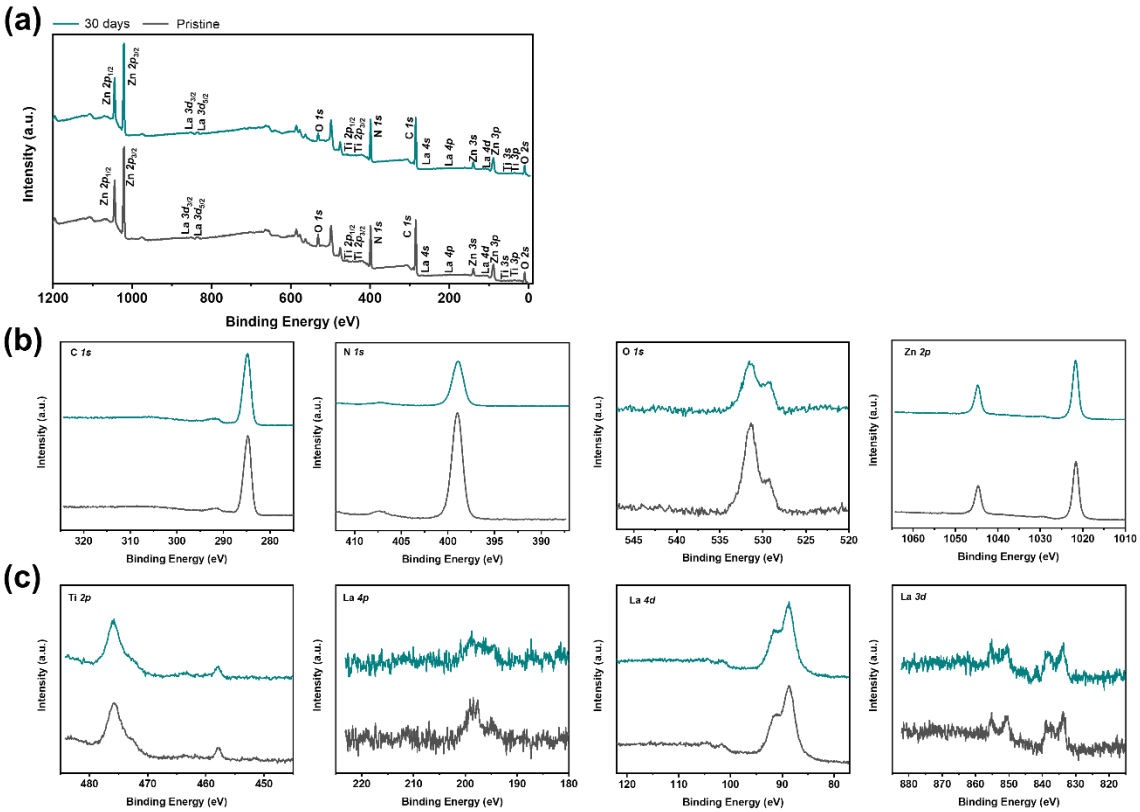

Fig. S18. XPS analysis of the membrane before and after 30 days of durability testing. (a) Survey spectra. (b) High-resolution spectra of Zn 2p, N 1s, and O 1s. (c) High-resolution spectra of LLTO-related elements for LLTO-containing samples.

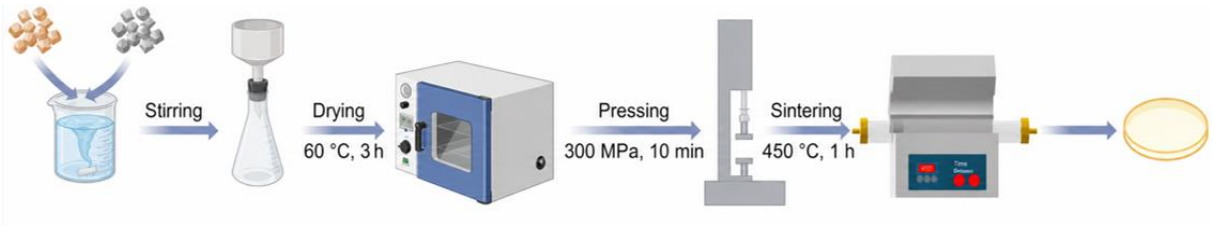

Fig. S19. Schematic illustration of the preparation process of $(LLTO)_x(ZIF\text{-}62\ glass)_{1-x}$ membranes. Created in BioRender. Feng, L. (2026) https://BioRender.com/1ayvrjx

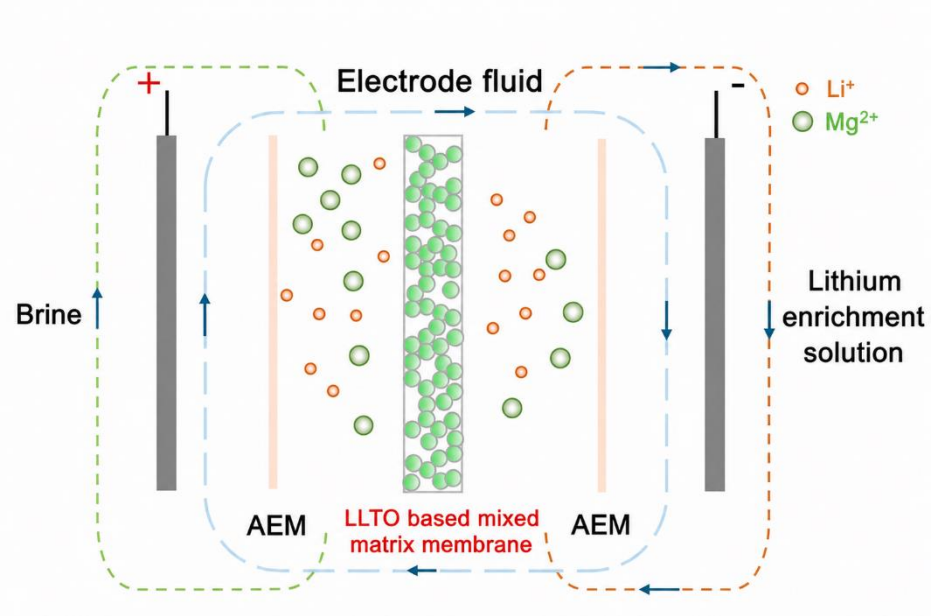

Fig. S20. Schematic illustration of the electrical extraction setup.

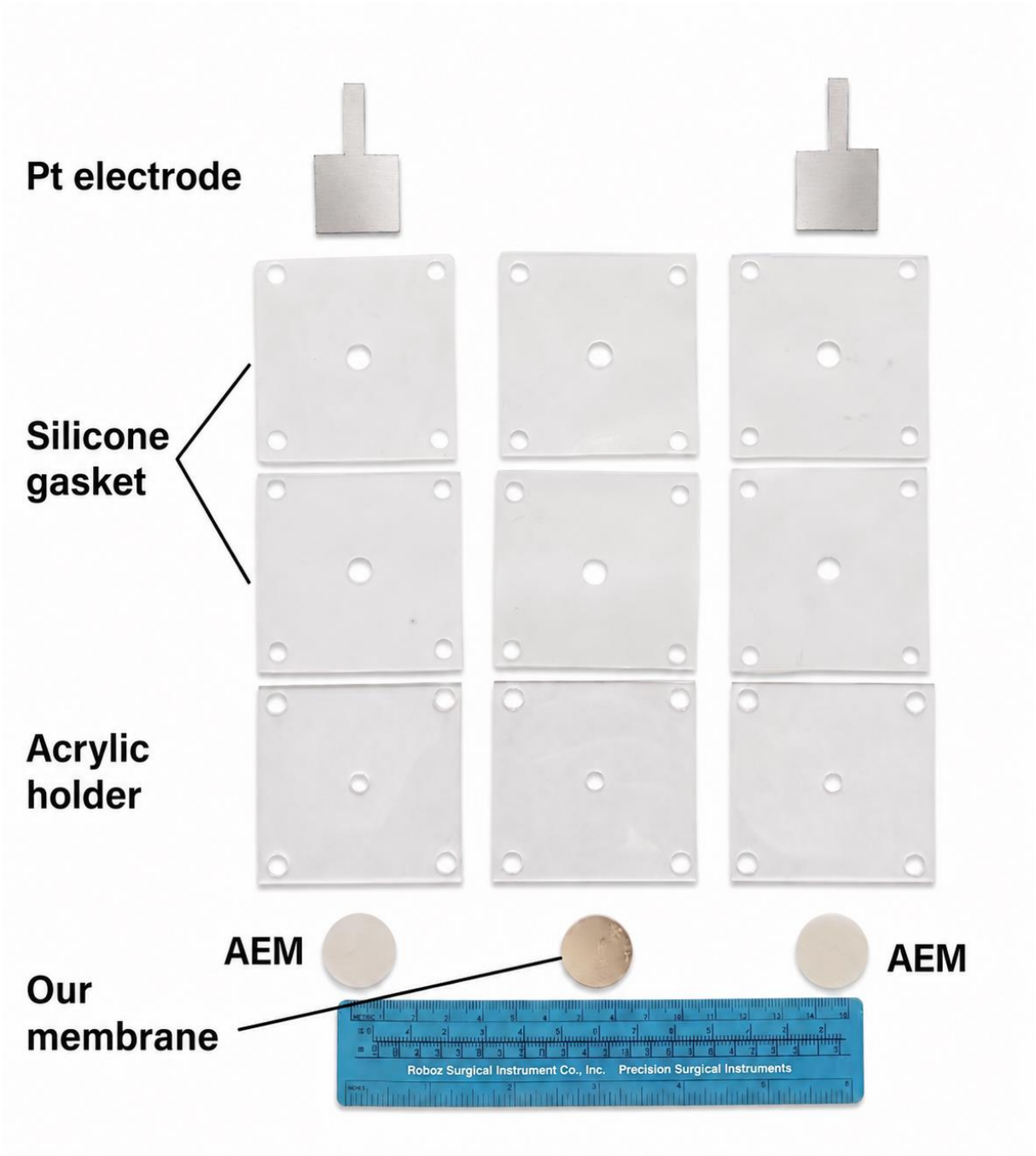

Fig. S21. Photo of the disassembled electrochemical cell components.

Table S1. Ionic composition of feed solutions used in lithium extraction tests.

Ionic Composition (ppm)	Li^+	Na^+	K^+	Mg^{2+}	Ca^{2+}
Red Sea	0.21	12356.40	746.56	1565.16	483.59
Dead Sea	47.42	2781.40	1754.39	133243.9	42419.11
Great Salt Lake	30.58	50995.13	3286.77	6623.92	538.91
Upper Rhine Graben	281.91	29738.31	5172.27	134.78	11334.15

Table S2. Comparison of lithium extraction performance with state-of-the-art membranes.

Material	Thickness (μm) & Support	Operating Conditions & Driving Force	Li in feed (ppm)	Mg in feed (ppm)	Mg/Li ratio	Li/Mg selectivity	Flux (mmol m^{-2} h^{-1})	Ref
LAGP	~200 - 500 (Ceramic pellet)	Galvanic cell (Concentration gradient)	200	12150	60.7	450	36.3	[5]
LAGP-PE	~20 (PE matrix) (Free-standing)	Electrolysis (4.7 V)	0.193	1209.6	6267	3.68×10^6	73.5	[6]
LATP/CA	~60 (Free-standing)	Electrodialysis (200 μA)	20.2	618.7	30.6	467.3	64.3	[7]
LATP/PVDF-HFP	~65 (Free-standing)	Electrodialysis (1.5 V)	0.036	390	10833	853.4	4.78	[8]
LATP/AEP	~1000 (Free-standing pellet)	Dialysis (Concentration)	694	2430	3.5	160	15	[9]
LLTO	~55 (Free-standing)	Electrodialysis (3.25 V)	0.21	1565	7452	45916	4.03	[10]
LLTO ($PVDF/TiO_2$)	~25 (On porous ceramic support)	Electrodialysis (3-12.5 V)	0.21	1700	8095	~87000	0.76	[11]
LLTO/PECH-DABCO	~100 (With nylon mesh)	Electrodialysis (2.0 V)	355	/	/	/	30.0	[12]
PA (Polyamide)	~55 (On PES support)	Nanofiltration (4 bar)	8.3	498	60	4147	70.3	[13]
HMO-S/PEEK	~100 - 150 (Free-standing)	Electrodialysis (constant voltage)	694	2430	3.5	3.1	3236	[14]
LLTO/ZIF-62 glass	~100 (Free-standing)	Electrodialysis (1.2 V)	0.21 47.42 30.58 281.91	1565 133243 6623 134	7453.1 2809.8 216.6 0.47	59564 17671 2916 506	0.69 4.96 4.19 16.02	This work

Table S3. Comparison of processing conditions, mechanical robustness, and lithium extraction performance between this work and conventional LLTO membranes.

	Thickness	Processing	Mechanical robustness	Li Flux	Normalized Li flux (100 μm)	Li/Mg Selectivity	Ref
LLTO	~55 μm	1275℃/8h	0.066% of flexural strain	4.03	2.22	~45000	[10]
LLTO	~25 μm (with support)	1250℃/6h	Requires support	0.76	0.19	~87000	[11]
LLLTO/ ZIF-62 Glass	~100 μm	450℃/1h	0.28% of flexural strain	0.69	0.69	~59000	This work

References

1. Last B, Thouless D. Percolation theory and electrical conductivity. *Physical review letters* **27**, 1719 (1971).

2. Sutorik A, Cooper C, Green M, Wolfenstine J, Gilde G. The Effect of Different La-Containing Starting Materials on the Synthesis, Sintering, and Li+-Conductivity of Li3xLa2/3-xTiO3. *JOURNAL OF CERAMIC SCIENCE AND TECHNOLOGY* **4**, 59-68 (2013).

3. Banerjee R*, et al.* High-throughput synthesis of zeolitic imidazolate frameworks and application to CO2 capture. *Science* **319**, 939-943 (2008).

4. Angell CA. Dynamic processes in ionic glasses. *Chemical Reviews* **90**, 523-542 (1990).

5. Zhang G*, et al.* Spontaneous lithium extraction and enrichment from brine with net energy output driven by counter-ion gradients. *Nature Water* **2**, 1091-1101 (2024).

6. Yang J*, et al.* Lithium Metal Recovery from Sea Water by a Flexible and Scalable Membrane with Lithium-Ion Exclusive Channels. *Angew Chem Int Ed Engl* **63**, e202411957 (2024).

7. Seo D, Lee J, Kong SR, Sim G, Park Y. Selective lithium extraction from salt-lake brine using LATP-incorporated cellulose membranes in electrically driven systems. *Journal of Membrane Science* **718**, (2025).

8. Shen K*, et al.* Flexible LATP composite membrane for lithium extraction from seawater via an electrochemical route. *Journal of Membrane Science* **671**, (2023).

9. Ma H, Xia Y, Wang Z, Xu T, Simon GP, Wang H. Dual-Channel-Ion Conductor Membrane for Low-Energy Lithium Extraction. *Environ Sci Technol* **57**, 17246-17255 (2023).

10. Li Z*, et al.* Continuous electrical pumping membrane process for seawater lithium mining. *Energy & Environmental Science* **14**, 3152-3159 (2021).

11. Liu H*, et al.* Electrodialysis Extraction of Lithium from Seawater Using Solid-State Electrolyte-on-Ceramic Membrane with High Aerial Capacity. *ACS Sustainable Chemistry & Engineering* **13**, 9621-9629 (2025).

12. Guo L-P, Guo Z-Y, Wang J, Zhang P-P, Huang Z-H, Ji Z-Y. Flexible lithium selective composite membrane for direct lithium extraction from high Na/Li ratio brine. *Journal of Membrane Science* **703**, (2024).

13. Peng Q*, et al.* Extreme Li-Mg selectivity via precise ion size differentiation of polyamide membrane. *Nat Commun* **15**, 2505 (2024).

14. Zhang J*, et al.* Hybrid Cation Exchange Membranes with Lithium Ion-Sieves for Highly Enhanced Li+

Permeation and Permselectivity. *Macromolecular Materials and Engineering* **304**, (2018).